JOURNAL OF PROPULSION AND POWER
Vol. 19, No. 3, May–June 2003

Scalability for Rocket Nozzle Flows Based on Subscale and Full-Scale Testing

Gerald Hagemann,* Jan Alting,† and Dieter Preclik‡
Astrium GmbH, 81663 Munich, Germany

When flow separation and side-load behavior is investigated for different nozzle concepts or when design considerations for advanced nozzle concepts are experimentally screened, the initial experimental effort is generally limited to subscale experiments with high-quality diagnostics. However, one fundamental question always arises: How should these test results be scaled to a potential full-scale design or application? Different approaches exist, including the use of characteristic numbers for normalization and analytical and numerical models. It is shown that analytical models, being based on physical origins and dominated by inviscid flow phenomena, may result in high accuracy for full-scale prediction. In contrast, it is shown that for flow regions dominated by viscous effects significant differences between cold- and hot-gas experiments are observed, which makes a direct scaling from cold-gas subscale to hot-gas full-scale difficult. For scaling, an intermediate step in the scaling rationale with hot-firing tests is foreseen. Demonstrated by results from hot-firing tests with Vulcain subscale nozzles, it is shown that a geometrical scaling is possible for similar hot-gas flow properties. These test results, obtained with a 40-kN thrust chamber at representative combustion chamber operation conditions, are presented and discussed in detail.

Nomenclature

F	=	side-load force
$H0$	=	time, instant of ignition
M	=	side-load torque, Mach number
m	=	mass
o/f	=	mixture ratio
PR	=	pressure ratio
p	=	pressure
r	=	radius
T	=	temperature
x, y, z	=	coordinate
δ	=	boundary-layer thickness
ε	=	area ratio, A/A_{throat}

Subscripts

a	=	ambient
c	=	combustion chamber
e	=	exit
i	=	incipient
p	=	plateau
SL	=	side load
sp	=	specific
sep	=	separation
throat	=	throat
w	=	wall

Introduction

WITH the need to evolve the European launcher family Ariane 5 to meet the future market requirements, its propulsion systems first have to be improved. Measures such as the introduction of the new core-stage Vulcain 2 engine or the new cryogenic upper stage with the HM-7 gas generator engine as a first step and the Vinci expander cycle engine in a next step are examples for these ongoing activities.

In the development of future launcher propulsion systems, the performance increase is, apart from the cost-reduction aspect, the most demanding and promising issue. Therefore, in rocket propulsion technology programs such as the 1996–2000 German technology program, "Nationales Technologieprogrammfuer kryogene Antriebe" (TEKAN), or the 2000–2003 German technology program "Ausgewaehlte Systeme und Technologien fuer zukuenftige Raumfahrt-Anwendungen" (ASTRA), different topics are being investigated to evaluate their potentials.[1,2] The spectra includes engine cycles, new manufacturing processes, new materials, and advanced concepts for the engine's main components injector, combustion chamber, and nozzle. Investigations include analytical, numerical, and experimental work.

In Europe, high area ratio nozzle concepts are envisaged for the next generation Vulcain engine to increase thrust chamber performance. In this context, a European working group has been set up to investigate the technological aspects covering separation and side-load characteristics of such nozzle concepts with flow separation control devices, FSCD. Within the framework of this FSCD program, partners from European industry (SNECMA, Volvo Aero Corporation, and Astrium), from space research establishments in France (ONERA, LEA Poitiers), Germany (DLR, German Aerospace Research Center), from the European Space Technology and Research Center (ESTRC), and from the French Space Agency, Centre National d'Etudes Spatiales (CNES), have tested different nozzle concepts at various facilities.

With respect to advanced rocket nozzle concepts, these type of experiments are typically conducted first at the cold-gas laboratory level, which allows for most cost-effective research and comparison of different configurations. An example for this is the screening of the various design considerations.[3–6] Obtained cold-gas test results are also used for model development and validation. However, with regard to full-scale engine development, the differences in both gas composition and in scale do not allow for a direct scaling of subscale test results to full scale. Different approaches for prediction from subscale to full scale may be followed, including the use of 1) subscale test data normalized by characteristic numbers also representative of full scale (based on Mach or Reynolds number analogy), 2) analytical models describing the underlying physical processes being responsible for specific flow phenomena,

Received 18 June 2002; revision received 6 November 2002; accepted for publication 6 November 2002.

*Project Manager, Research Engineer, Space Infrastructure Division. Member AIAA.
†Project Manager, Research Engineer, Space Infrastructure Division.
‡Head, Advanced Programmes, IP31, Space Infrastructure Division. Member AIAA.

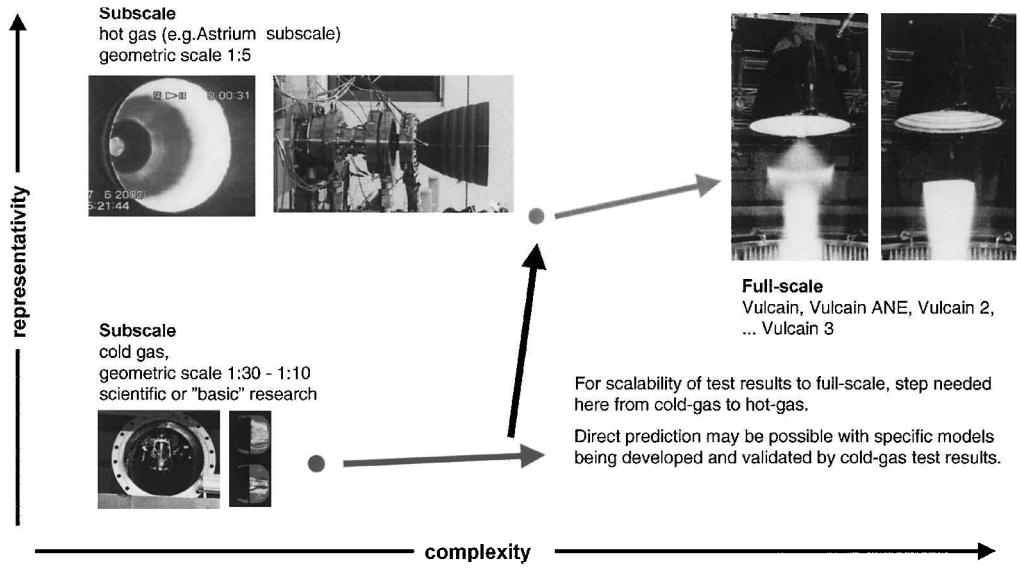

Fig. 1 Scalability logic.

3) numerical methods accounting for physical processes being involved, or 4) subscale hot-gas tests at similar operation conditions and representative geometric scale. This paper deals with the scalability discussion, specifically addressing rocket nozzles.

Each approach comprises specific characteristics. The differences in gas composition and geometric scale make it difficult to base the scaling rationale on a single dimensionless number for normalization.

Reliable analytical and/or numerical models may be used to account for the different physical phenomena involved. It has been shown in various publications that for some flow phenomena, such as the side loads due to a change in separation pattern for specific types of conventional rocket nozzles, analytical models allow for an accurate prediction toward full scale. However, the reliability of analytical models is currently questionable, especially for flow phenomena in advanced rocket nozzles including highly transient processes, such as the side loads induced by the transition process in dual-bell nozzles.

Therefore, for an accurate and reliable extrapolation toward full scale, the test logic at Astrium, foresees subscale hot-firing tests at representative conditions as the most promising concept initially evaluated at the laboratory level. Experience gained in industry shows that these subscale hot-firing tests at typical full-scale operational conditions, that is, identical injection elements, similar element patterns, and oxidizer/fuel injection conditions as in full-scale, can be used for representative geometric scaling to full scale. (The Astrium, subscale injector head includes three injector rows with a total of 19 injectors,[1,2] leading to a combustion chamber diameter of 80 mm with a close to one-fifth, geometric scale when compared to full scale. Similar hardware sizes are also used at Aerojet; Pratt and Whitney, United Technologies Corporation; and Rocketdyne for subscale thrust chamber technology tests.[7,8])

These hot-firing tests are useful for further model development and validation because they close the gap in the uncertainty of models developed exclusively from cold-gas laboratory tests and directly applied to full scale. This test philosophy is illustrated in Fig. 1. It is discussed for conventional parabolic nozzle extension, for which the entire spectra of test results from cold-gas subscale to full-scale engine test data, analytical models for side-load behavior, and numerical flowfield simulations are available. Before this scalability discussion, a brief summary of characteristic flow phenomena for parabolic rocket nozzles is given.

Flow Phenomena in Parabolic Nozzles

In general, the exit wall pressure $p_{w,e}$ of a rocket nozzle operating from sea level to high altitude is chosen high enough to prevent flow separation inside the nozzle.[9–11] The additional requirement of high-vacuum performance leads to an overexpanded, but attached nozzle flow at takeoff, that is, sea-level condition.

At the nozzle exit, the lower pressure of the exhaust gases is adapted to the higher ambient pressure by means of an oblique shock system. Mainly as a result of the exit pressure ratio p_e/p_a and exit Mach number M_e, three different plume patterns are observed: a regular reflection, a Mach reflection with a Mach disk, or a so-called cap-shock pattern. The latter shock pattern exists in the plume of thrust-optimized rocket nozzles and nozzles with parabolic contours featuring an internal shock induced in their throat areas. Recent investigation on the cap-shock pattern have shown that this specific plume pattern is an inverse Mach reflection of the internal shock at the centerline.[12] As an example, this cap-shock pattern is clearly visible in the plume of the Vulcain engine. In Fig. 1, the top right side shows the running Vulcain engine at two different operational conditions, showing the cap-shock pattern (left), and the Mach disk (right). A more detailed investigation on the cap-shock pattern is given in Ref. 12.

If the pressure ratio of the exit wall pressure to the ambient pressure is below a certain level, that is, $p_{w,e}/p_a \sim$ 0.3–0.4, the flow regime within the nozzle is different from vacuum conditions because the flow separates from the nozzle wall upstream of the exit plane. Two different separation patterns may exist, the free shock separation (FSS), where the flow separates from the wall and further propagates as an annular freejet, or the restricted shock separation (RSS), where the flow reattaches to the nozzle wall downstream of the initial separation point. Figure 2 shows the phenomenology and wall pressure profiles for FSS and RSS. Numerical and analytical studies of nozzle flows have shown that the existence of the cap-shock pattern is responsible for the transition from FSS to RSS.[9–12] The transition process itself is impulsive and highly three dimensional. Consequently, severe lateral forces are induced.

A further side-load origin is the final retransition from RSS to FSS. Recent investigation have shown that these transitional side-loads are much higher than sideloads due to random pressure pulsations at the separation point as well as in the separated flow region being typical for conical or truncated ideal nozzles.[13]

The quantitative prediction of both the flow separation characteristic during start-up and shut-down, and the maximum side loads expected during transient engine processes is of importance to define the thrust chamber structure and to ensure its mechanical integrity under worst-case conditions. Therefore, prediction methods must be accurate. These methods may be based on analytical or numerical models, or simply on subscale test data. In the following, different approaches highlighted in the "Introduction" will be discussed using the transition process in separation pattern from FSS to RSS

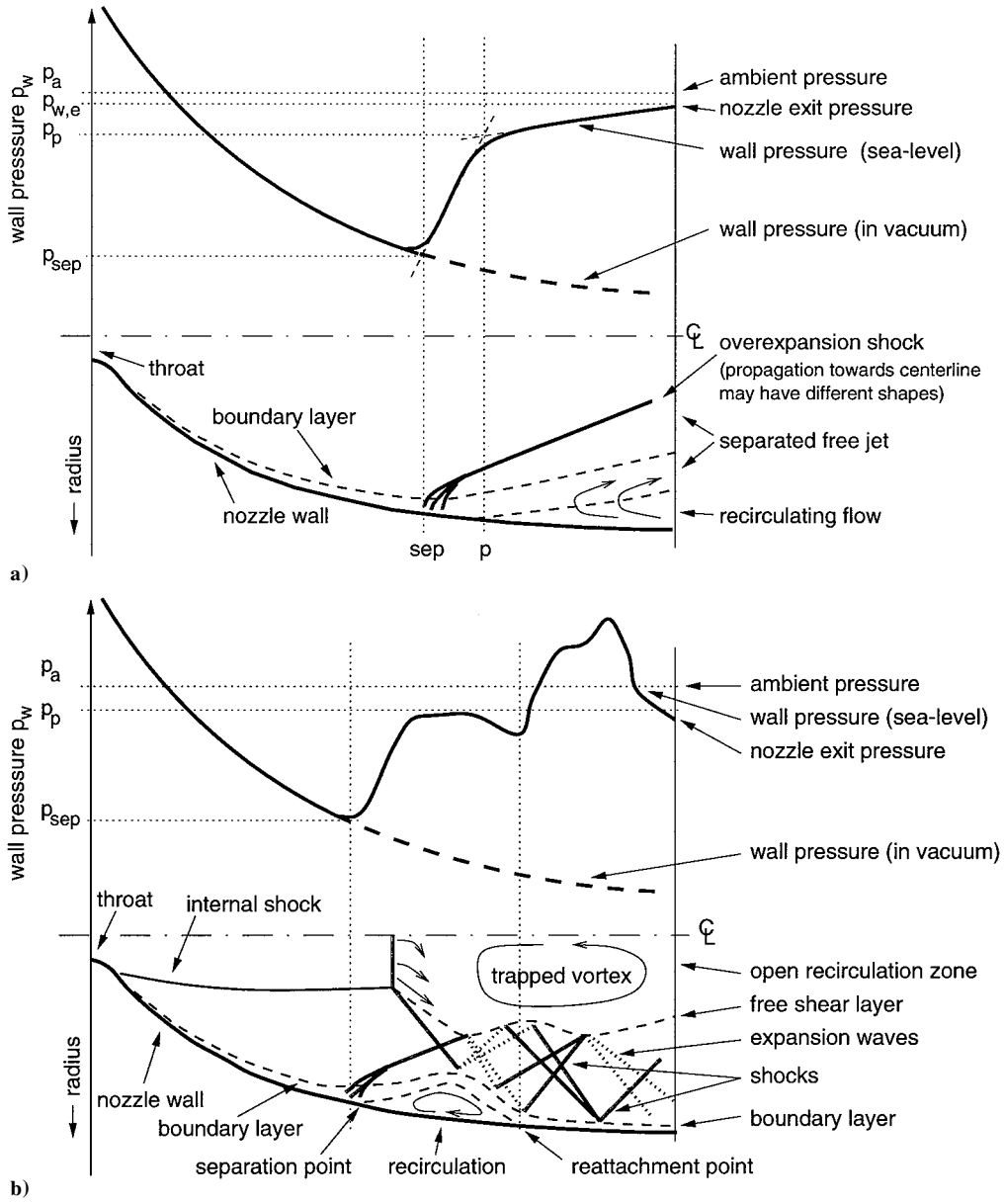

Fig. 2 Phenomenologics a) FSS and b) RSS.

as an example. This discussion will include the specific cap-shock structure and the transitional side loads for subscale cold-gas, subscale hot-gas, and for full-scale engine tests. The Vulcain nozzle will serve as a full-scale reference test hardware and is briefly described.

Full-Scale Engine Tests

The engine of the Ariane 5 cryogenic core stage, Vulcain, was developed under the responsibility of SNECMA in France, which shares the activities with more than 30 partners in Europe. Astrium, is responsible for the thrust chamber consisting of gimbal joint with cross-type cardan, injector, combustion chamber, and nozzle extension. The injector and combustion chamber are manufactured at Astrium, the nozzle extension is manufactured at Volvo Aero Corporation. The nozzle extension itself is of parabolic type, with an exit area ratio of $\varepsilon = 45$, which allows for full-flowing operation at sea level for nominal combustion chamber conditions, that is, a mixture ratio $o/f = 5.89$ and a combustion chamber pressure around $p_c = 100$ bar. Because of its parabolic contour, a transition from FSS to RSS and vice versa occurs during start-up and shut-down. A detailed description of the transient flow processes in the Vulcain nozzle is given in Ref. 10. The initial transition from FSS to RSS during start-up is considered in more detail later. Test results have shown that this transition occurs at a chamber pressure of $p_c = 35$–40 bar. The maximum side load measured in Vulcain qualification tests is caused by this transition. Figure 3 illustrates the flow asymmetry during the transition from FSS to RSS that is responsible for this side-load peak.

Cold-Gas Laboratory Test Campaign

Within the framework of the European FSCD program, several nozzle concepts were tested at various facilities.[4–19] For example, at DLR, German Aerospace Research Center, Lampoldshausen, a thrust-optimized parabolic (TOP) and a truncated ideal contour (TIC) nozzle with equal vacuum performance were tested. See Ref. 13 for a detailed description of the test campaign and results. Table 1 summarizes geometric design values.

Figure 4 shows both plume patterns observed in the experiments, the classical Mach disk for the truncated ideal nozzle, and the cap-shock pattern for the parabolic nozzle. Test results in Fig. 5 clearly indicate that side loads in the parabolic nozzle extension due to the transition from FSS to RSS and vice versa are much higher than side loads measured in the truncated ideal nozzle. Despite this clear trend, the cold-gas test results cannot be reliably used for direct extrapolation to full-scale due to two main differences.

Table 1 Design data[a] for cold-gas nozzles with TIC and TOP

Geometric design data	TIC	TOP
Throat radius, mm	10	10
Area, ratio	20.66	30
Nozzle length, mm	148.3	125

[a]Driving gas pressure ratio nitrogen, $\kappa = 1.4$ and PR $1 < p_c/p_a < 60$.

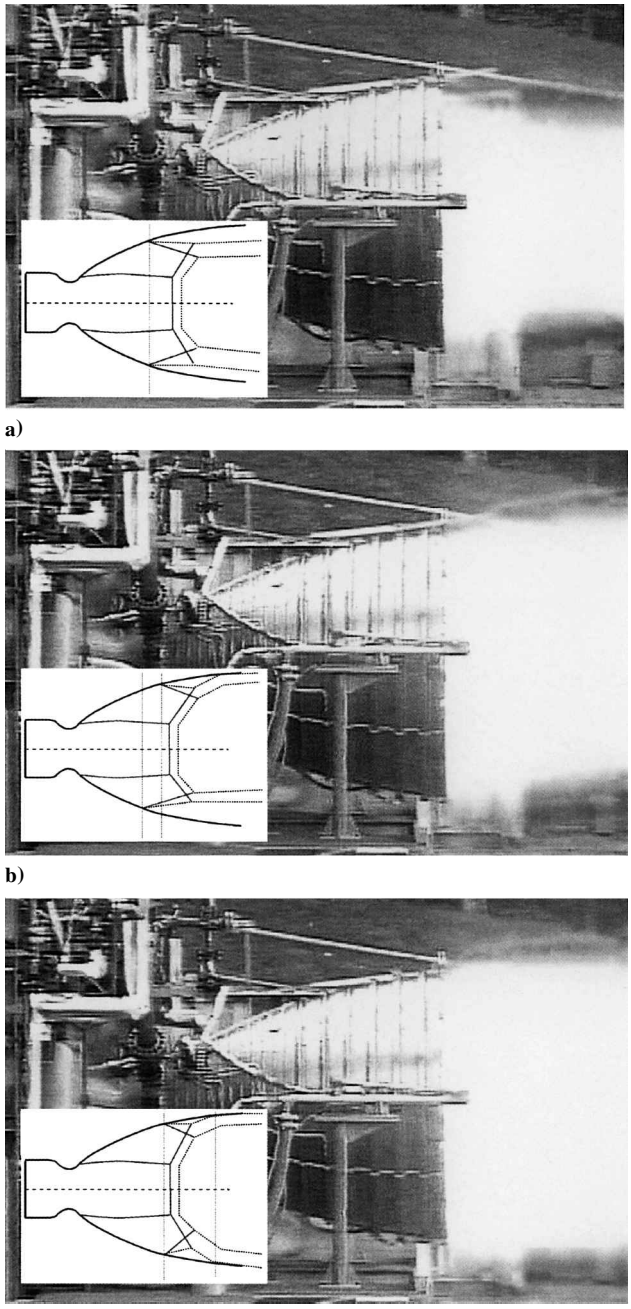

Fig. 3 Video analysis of Vulcain thrust chamber start-up at $p_c/p_a \sim 40$, three subsequent images with time interval of 0.04 s: a) full FSS, b) RSS in upper nozzle part, FSS in lower nozzle part, and c) full RSS.

1) Geometric scale with respect to full-scale is only of the order of 1/30th–1/10th.

2) Gas composition is significantly different from typical full-scale test conditions.

Compared to hot-firing results, the shock positions are different in cold-gas testing for differences in specific heat ratios. Furthermore, the energy balance differs significantly due to the combustion process, which leads to different momentum values as well.

Table 2 Quantitative comparison of experimental and model data for transition FSS to RSS and resulting side-load torque

Tests	Transition FSS–RSS (experiment/model)	Side-load torque due to tansition (experiment/model)
DLR P6 TOP	0.97	0.92
Volvo FOI S1	0.94	1.09
Volvo FOI S3	1	0.93
LEA TOC	0.85	0.99
C/SiC subscale	1.03	Experiment value not available
Vulcain full-scale	1.03	1.02

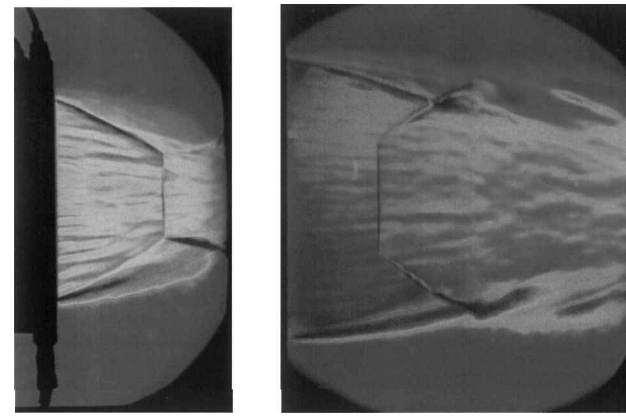

Fig. 4 Different plume pattern in P6.2 subscale nozzles, visualized by color schlieren technique: a) Mach disk in plume of TIC and b) cap-shock pattern in plume of TOP (courtesy DLR, German Aerospace Research Center).

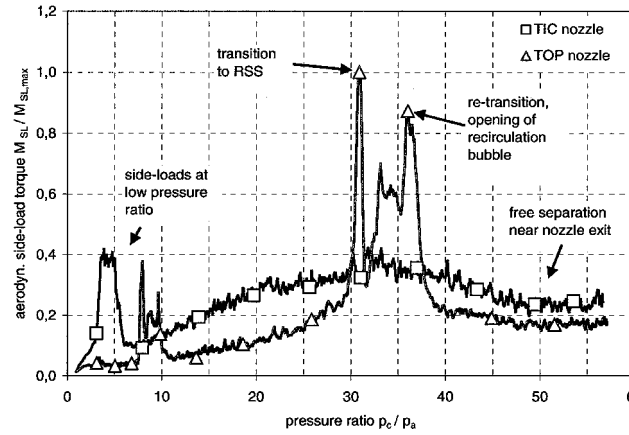

Fig. 5 Comparison of averaged side-load torque for the truncated ideal and the thrust-optimized nozzle for simulated start-up (courtesy DLR, German Aerospace Research Center).

As a consequence, models to predict the full-scale transition process and the resulting side-load had to be developed. In Refs. 9, 12, 14 and 16 details are given for this model development based on an analytical prediction of the cap-shock structure at a prescribed pressure ratio. A comparison of the cap-shock structure prediction shown for the P6.2 thrust-optimized parabolic contour (TOP) nozzle at a pressure ratio of $p_c/p_a = 68$ is given in Fig. 6 (Ref. 14). In the model it is assumed that, at the instant of transition where the maximum side load occurs, one-half of the nozzle features FSS while the other half features the RSS. The final side-load calculation results from a wall pressure integration as shown in Figs. 7 and 8 and takes into account the momentum of the initially separated jet hitting the wall at the nozzle exit for that part of the nozzle featuring RSS. In Table 2, experimental test data are compared with model results. A fairly good agreement is observed, including the full-scale Vulcain test case.

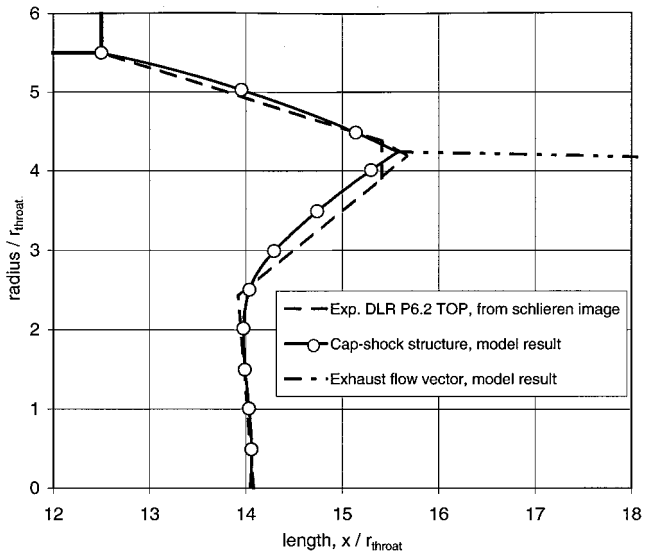

Fig. 6 Analytical prediction of cap-shock structure, P6.2 TOP nozzle, PR $p_c/p_a = 68$.

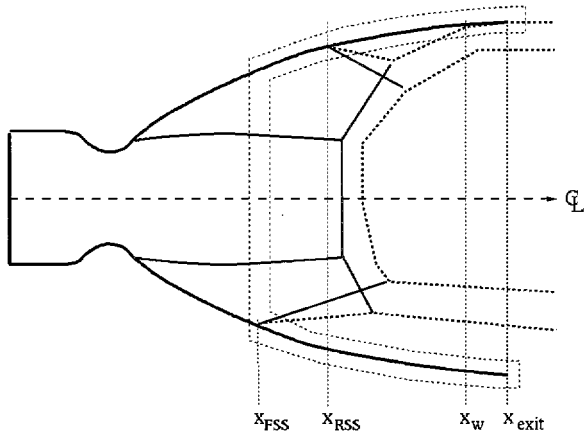

Fig. 7 Control surface for momentum balance for side-load model: . . . ., control surface for momentum balance and ——, shocks.

The transitional side-load is mainly governed by inviscid flow phenomena, that is, the momentum balance across the oblique shock system of the cap-shock pattern and the resulting wall pressure integration. From the agreement shown in Table 2 between the cold-gas test data and model results, it can be concluded that models primarily based on physical phenomena dominated by inviscid effects and, therefore, independent of geometric size have the potential for serving as an accurate and reliable prediction tool. [Note that for inviscid hot-gas flows the geometric size influences the chemical reaction rates. However, it has been shown that for hydrogen/oxygen systems, as considered here, these chemical nonequilibrium effects are regarded as a second-order effect and can be neglected for chamber pressures above 50 bar (Ref. 20).]

In contrast, it is well documented in the literature that analytical approaches for flow phenomena dominated by viscous effects, for example, the prediction of the flow separation itself, still lack sufficient accuracy.[9,12,16,17]

Hot-Firing Test Campaign

Within the framework of the TEKAN and ASTRA programs, two ceramic nozzle extensions were designed, manufactured, and tested at the F3 test bench in Ottobrunn, Munich, and at the European P8 facility at DLR, Lampoldshausen.[21] Key objectives for the choice of a ceramic subscale nozzle demonstrator were 1) to ensure thermal and mechanical integrity of the radiation-cooled C/SiC nozzle extension at representative ground-stage operation conditions; 2) to examine the flowfield in the expansion regime by video images, thermography, and pressure measurement devices; and 3) to demonstrate geometric scalability of these subscale tests directly to full scale.

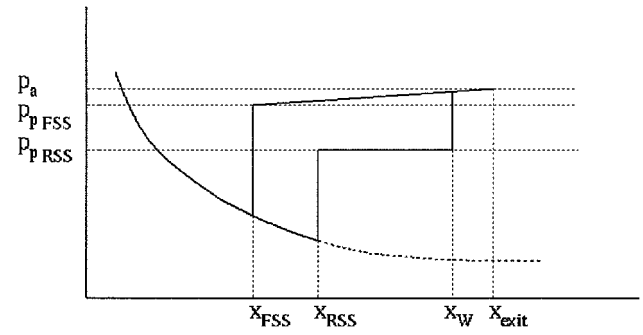

Fig. 8 Wall pressure distribution along control surface for momentum balance.

The thrust chamber hardware test setup consists of 1) 19-element injector head, 2) cylindrical combustion chamber with 80 mm diameter, 3) profiled throat section with scaled Vulcain contour and with 50.6-mm throat diameter (one-fifth geometric scale), 4) graphite interface section for mounting of ceramic nozzle extension, and 5) ceramic nozzle extension with scaled Vulcain contour.

The subscale test specimen is shown in Fig. 9. The combustion chamber's design pressure for the presented hardware setup is $p_c = 100$ bar at a mass flow rate of $\partial m/\partial t \approx 9$ kg/s, resulting in a 40-kN vacuum thrust level. The ceramic nozzle extension starts at an area ratio of $\varepsilon = 5$. Two different extensions were tested with exit area ratios of $\varepsilon = 30$ and 45, the latter being the same as for Vulcain. The objective for the shortened design with $\varepsilon = 30$ was to allow for an operation under full-flow conditions down to a chamber pressure of $p_c = 40$ bar and thereby avoid the transition to RSS. Within the design process, it was shown that a steady-state operation under restricted shock separation with its characteristic reattached supersonic flow exposes the nozzle wall to tremendous heat loads. The long nozzle extension with $\varepsilon = 45$ was designed for steady-state operation at a minimum chamber pressure of $p_c = 75$ bar to avoid any long duration, steady-state operation under RSS. Detailed analysis and calculations were conducted to design the nozzle extensions to cope with both thermal and structural loads. Mechanical design load cases were 1) maximum side-load case at $p_c = 40$ bar (side-load value geometrically scaled down from Vulcain test experience) and 2) buckling load case at $p_c = 65$–70 bar with maximum integral pressure difference between highly overexpanded nozzle flow and ambience.

For the long nozzle extension, five stiffeners were installed providing the structural stability against buckling, that is, the nozzle load case with significantly lower pressure inside the nozzle compared to the ambient pressure. Figure 10 illustrates both nozzle extensions. A total of seven high-frequency pressure transducers with ceramic adapters were installed in the short nozzle, with four in a row as shown in Fig. 10. The remaining three transducers are mounted at the axial position of PNE1, corresponding to $x/r_{\text{throat}} = 8.6$, but at 90, 180, and 270 deg in the circumferential direction. (Here the throat radius r_{throat} is applied for normalization.) The ceramic adapters were flush mounted to the hot-gas side inner wall to avoid any step formation.

Hot-Firing Tests with Short Nozzle Extension

The short nozzle extension was tested in various test sequences, with steady-state operational points at $p_c = 35$, 60, and 70 bar chamber pressures. Mixture ratio was varied between $o/f = 5$, 6, and 7. Figure 11 shows a typical test image in which steady-state wall temperatures are not yet achieved. Reference 21 includes a detailed discussion on the different test sequences and test objectives.

Figure 12 shows details of averaged wall pressure data measured with the short nozzle extension. For comparison, Vulcain full-scale test data at different pressure ratios (PR) are also included, but

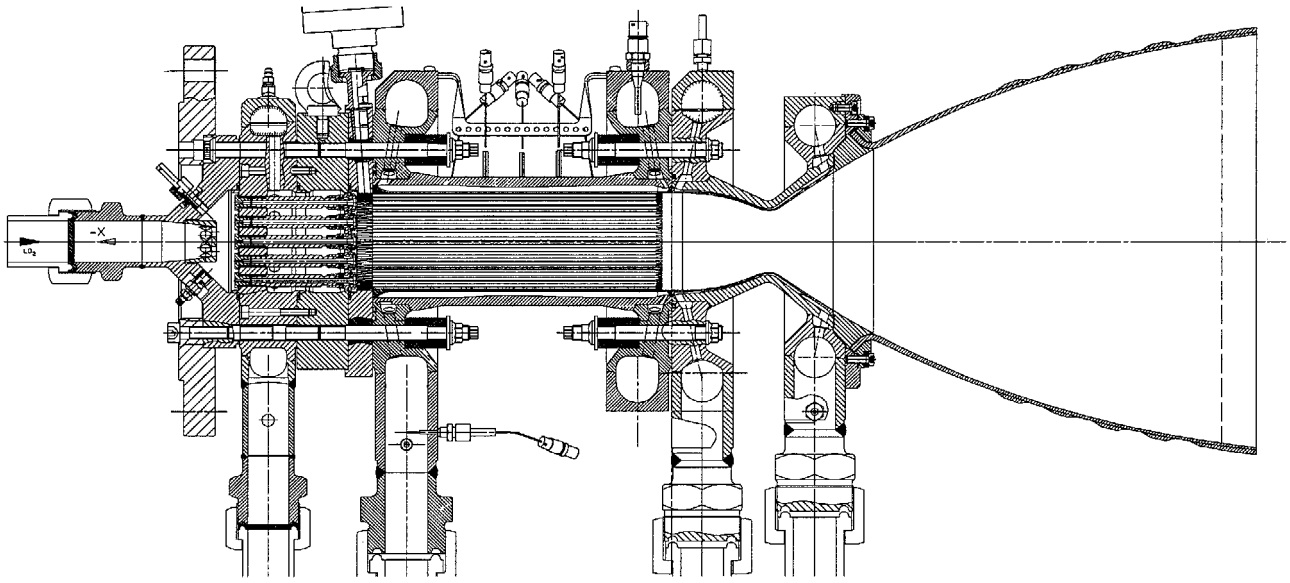

Fig. 9 Astrium, 40-kN subscale thrust chamber assembly with radiation-cooled ceramic nozzle extension.

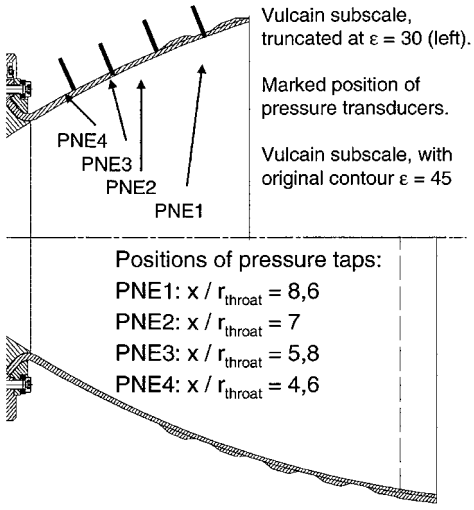

Fig. 10 Design of ceramic nozzle extensions (axial positions of pressure taps measured from throat).

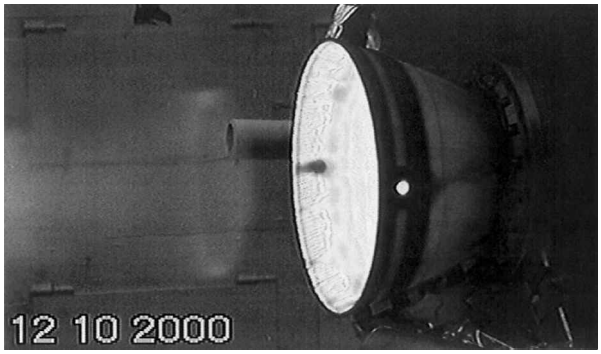

Fig. 11 Short ceramic nozzle extension at load point with $p_c = 60$ bar.

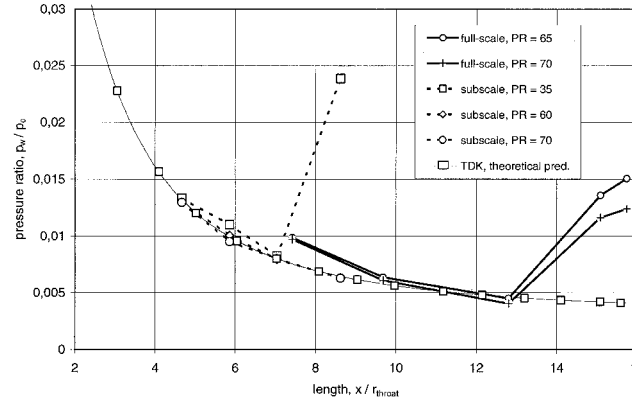

Fig. 12 Wall pressure measured in Vulcain full-scale nozzle and in short subscale nozzle.

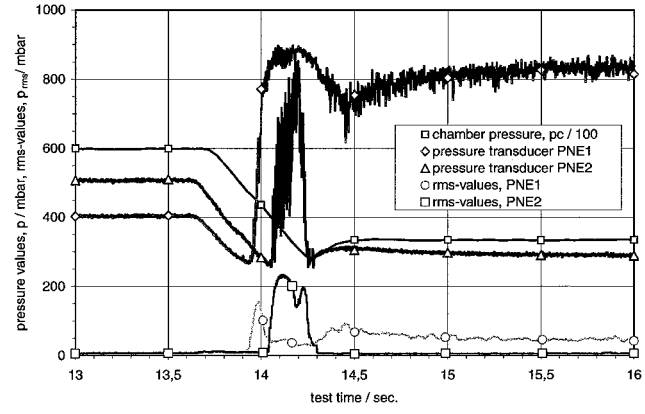

Fig. 13 Wall pressure data and corresponding rms values across separation region.

limited to values at which FSS was observed. The comparison of experimental and numerical data, the latter extracted from a turbulent TDK vacuum flowfield simulation including chemical nonequilibrium effects,[22] shows good agreement for attached flow conditions. In fact, in conventional nozzles the viscous effects influenced by geometric scale are limited to the thin near-wall boundary layer; the wall pressure itself is dominated by inviscid core flow evolution. In conclusion, the geometric scale has no influence on vacuum wall pressure profile, under the condition of similar core gas composition (excluding the aforementioned second-order effect of geometric size on chemical reaction rates).

The comparison of the four circumferential distributed hf-sensors in the most downstream plane indicates attached flow during all load points except the $p_c = 35$ bar case. The hf analysis reveals further interesting results for the nozzle flow behavior. Figures 13 and 14 show typical rms levels across the incipient separation zone.

In the incipient separation zone between x_{sep} and x_p, the flow physically detaches from the nozzle wall. The location of the separation point is the subject of hf oscillations between x_{sep} and x_p. The shock/boundary layer interaction causes the pressure increase to the plateau pressure value p_p. Farther downstream of x_p, the flow is fully separated, and ambient air is entrained into this separated region.

During steady state with fully attached flow, the rms value is very low, with $p_{rms} < 5$ mbar. This is the case for PNE1 and PNE2 for a chamber pressure of $p_c = 60$ bar, corresponding to $13 < t < 13.7$ s in Fig. 13. For PNE1, pressure values clearly indicate separated flow during down ramping and the subsequent $p_c = 35$ bar load point. The rms values for this time interval approach a value of ≈ 50 mbar, which is 10 times higher than for the fully attached case, but approximately 4 times lower than for PNE2, which is just

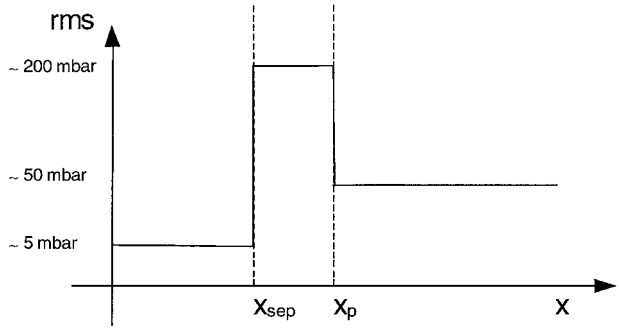

Fig. 14 Pressure signal across-separation region rms level.

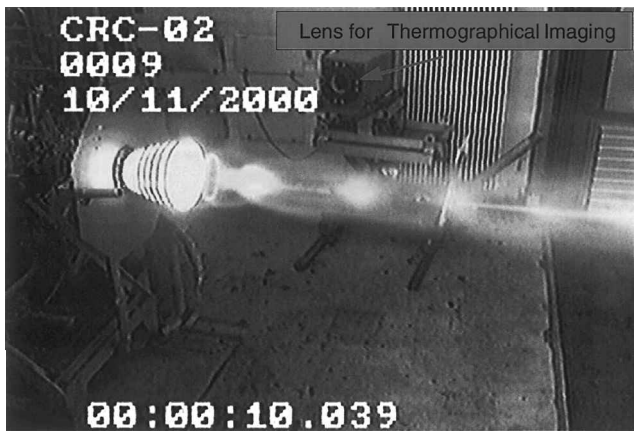

Fig. 15 Long C/SiC subscale nozzle extension at $H0+10$ s; exhaust plume with cap-shock pattern and shock reflection.

at the beginning of the incipient separation region during the lowest operational point with $p_c \approx 34$ bar, at $14 < t < 14.3$ s. In between, the rms value is ≈ 200 mbar. These levels are in agreement with published data.[23]

According to studies reported in Refs. 23–25, the length of the incipient separation region is of the order of two to three times the local boundary-layer thickness. For the correlation of these test data, a TDK flowfield simulation[22] was performed assuming the following conditions: chamber pressure $p_c = 35$ bar, mixture ratio $o/f = 6$, and radiation-cooled wall for nozzle extension.

As a result, a normalized boundary-layer thickness of $\delta/r_{throat} = 0.55$ was calculated at $x/r_{throat} = 7$, the position of PNE2. [The boundary-layer thickness is defined as the distance normal to the wall where $(u/u_\infty) = 0.995$ is reached. The nozzle throat radius r_{throat} is applied for normalization.] Thus, the incipient separation thickness would result in the following:

$$\Delta x_{i,sep} = x_p - x_{sep} = (2\text{–}3) \cdot \delta = (1.11\text{–}1.66) \cdot r_{throat}$$

The experimental data reveal an incipient separation length of $1.58 \cdot r_{throat}$, which correlates well with the earlier estimated values based on literature. However, recent cold-gas experiments[19] have revealed an incipient separation thickness of the order of $(10\text{–}20) \cdot \delta$ and, thus, one order of magnitude larger than for these hot-gas tests. This discrepancy has to be further investigated. However, it may indicate that for flow regions dominated by viscous effects, as is the case for the incipient separation region, cold-gas test data must be treated with care for direct comparison.

Analytical models for side loads due to pressure pulsations under FSS condition, as presented in Refs. 23 and 26, include this incipient separation thickness. A direct extrapolation from these subscale cold-gas results to full scale without further exploiting the reason for observed discrepancies with the presented hot-gas test results would result in far too high side loads predicted for full scale.

Hot-Firing Tests with Long Nozzle Extension

The long nozzle extension was tested in two test sequences, one with a maximum chamber pressure of $p_c = 40$ bar to investigate the transition process from FSS to RSS and a second that comprised only a single load point with $p_c = 80$ bar and $o/f = 6$ for the entire test duration of 32 s. The latter load point was sufficient to have a full-flowing nozzle extension (Fig. 15).

Figure 16 shows the transition process with a view from downstream looking back into the nozzle extension. The reattachment occurs first at the nozzle exit, visible by the sudden and intensive onset of radiation. Once the reattachment bubble is closed over the entire exit plane, the reattachment line shifts upstream to its stable position. The nozzle extension withstood the transition process

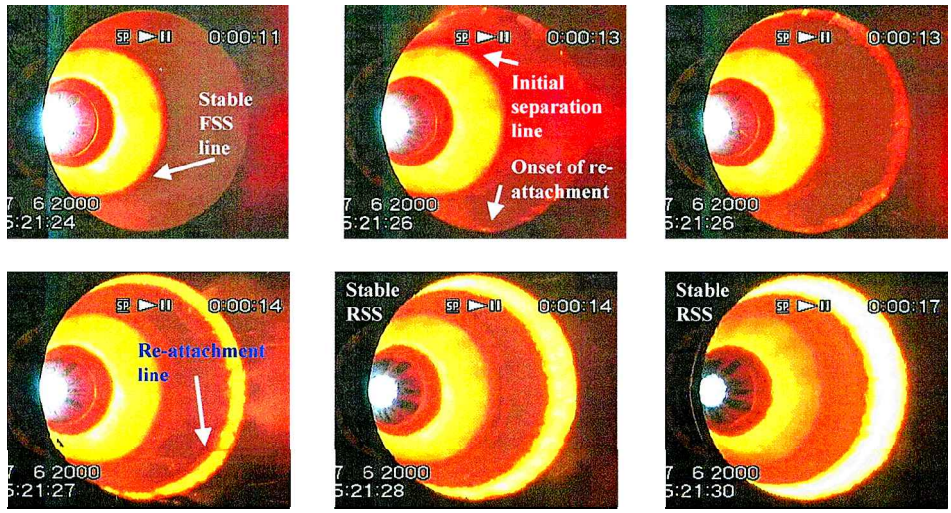

Fig. 16 Details of the transition process from FSS to RSS in the long Vulcain C/SiC subscale nozzle at $p_c = 40$ bar (from left to right and top to bottom).

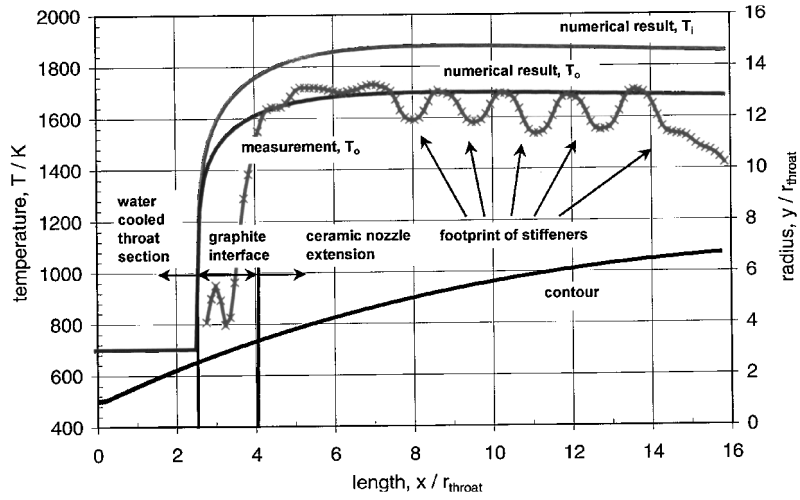

Fig. 17 Comparison of predicted and measured nozzle surface temperatures for long Vulcain C/SiC subscale nozzle, test CRC_02; T_p and T_i.

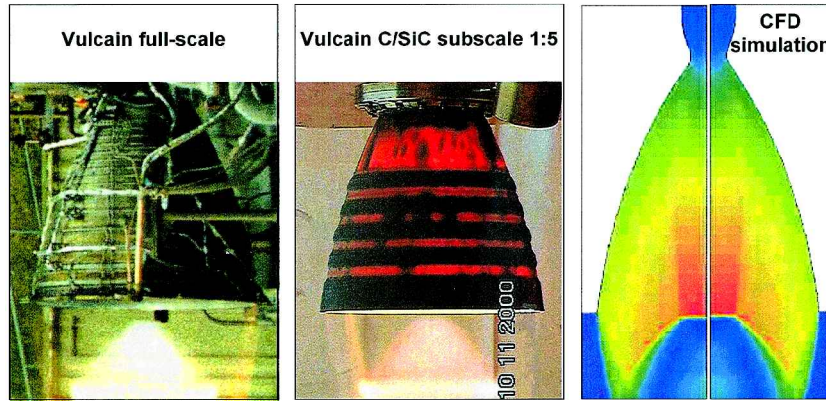

Fig. 18 Comparison of Vulcain type full-flowing nozzles at nearly identical operational conditions: a) full scale, b) long C/SiC subscale, and c) numerical simulation for full scale.

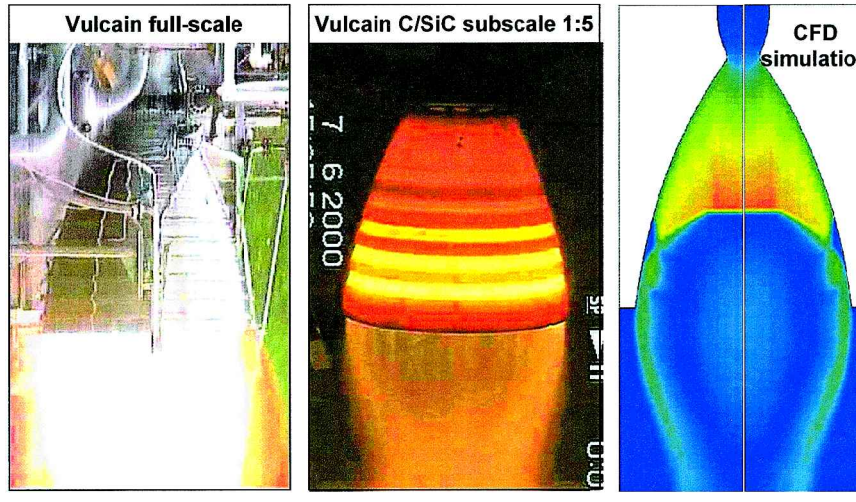

Fig. 19 Comparison of Vulcain type nozzles featuring RSS a) full-scale, b) long C/SiC subscale, and c) numerical simulation for full scale, $p_c/p_a = 40$.

without structural damage. It must be stressed that the transition itself took place at the PR predicted by the analytical model and also as expected from full-scale engine test data as shown in Table 2. Again, the transition and the resulting side force is mainly governed by the inviscid momentum balance across the oblique shock system of the cap-shock pattern. This oblique shock structure is practically the same for the subscale and full-scale nozzle flowfield, due to the similar contours and core gas properties. (This will also be demonstrated subsequently.) It is not surprising that flow structure and phenomena observed subscale and fullscale are practically equal. However, this does demonstrate that only subscale tests with similar hot-gas flow properties will allow for direct extrapolation toward full scale.

Figure 15 shows the high chamber pressure test with $p_c = 80$ bar at $H0 + 10$ s. The exhaust plume with the typical cap-shock pattern is clearly visible. Additionally, the thermographical imaging lens

Table 3 Characterization of various influence parameters on flow phenomena associated with flow separation and characterization of its representativity with respect to full-scale[a]

	Influence			Representative with respect to full-scale	
Effect	Viscid effects	Gas composition	Size	Cold tests	Hot tests
Shock shape		X		−	+
Shock pattern (e.g., cap-shock pattern)	x	X		o	+
Momentum balance across shock/shock interaction	x	X		+	+
Separation point location, including shock/boundary-layer interaction	X	X	x	−/o	+

[a]Symbols: x, influence of secondary order; X, influence of first order; +, fully representative, −, not representative; and o, limited representative.

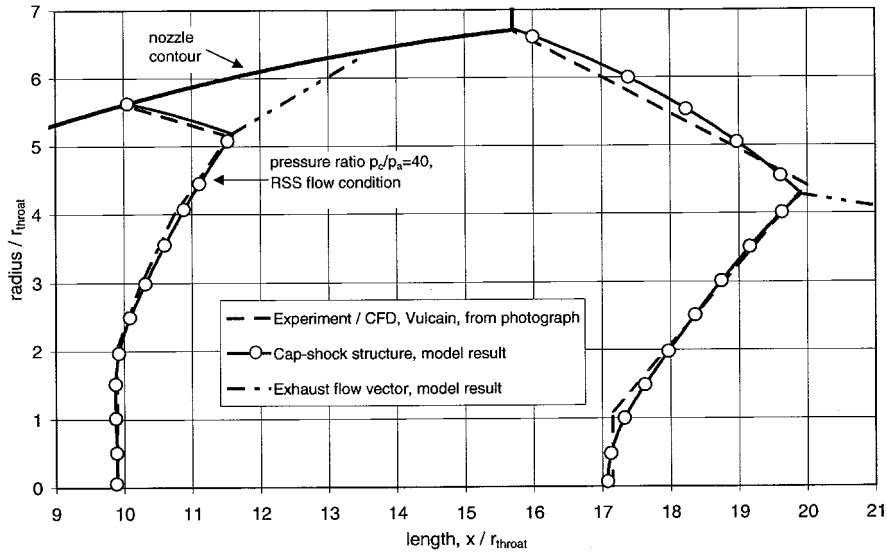

Fig. 20 Cap-shock structure in the Vulcain nozzle; analytical model result, experimental, and numerical result: $p_c/p_a = 40$ with RSS flow condition and $p_c/p_a = 90$ with full-flowing nozzle.

system is shown, orientated nearly perpendicular to the outer surface of the nozzle. The measurement data indicated that the temperature distribution reached steady-state conditions at about $H0 + 24$ s. For this steady-state condition, a numerical wall temperature prediction was calculated with the Astrium, Navier–Stokes code ROCFLAM. (See Ref. 27 for further details.) This simulation included the flowfield prediction, the modeled hot-gas side-wall heat transfer, the heat conduction in a wall of finite thickness, and the heat flux transferred by external radiation. The code has been extensively validated with wall heat flux data measured in a calorimeter combustion chamber in the regime up to $p_c = 70$ bar (Ref. 27).

The steady-state prediction for this operational point is presented in Fig. 17. Both solid lines represent the nozzle temperature prediction: the upper one, T_i is the inner wall value and the lower one, T_o is the outer wall temperature. The symbol-marked line is the nozzle's outside temperature measured by the thermographical imaging method. Although the values differ in the first graphite interface region ($2.5 < x/r_{\text{throat}} < 4$) where the measurement signal is disturbed due to mirror effects, the predicted temperature values agree very well with the measured ones. The shape of the measurement curve is caused by the stiffeners installed on the nozzle. These stiffeners nearly double the wall thickness and, thus, change the heat transfer profile. The stiffeners were not modeled here for simulation simplicity.

Comparison of Flow Pattern in Sub- and Full Scale

Figure 18 compares the flow pattern of the subscale nozzle with the Vulcain full scale and a computational fluid dynamics prediction. Details on the numerical method are included in Refs. 11 and 12. The cap-shock pattern is clearly visible in all three images and shows nearly identical shape. As mentioned before, this plume pattern results from the interaction of the recompression shock and the inverse Mach reflection of the internal shock. (Also see Ref. 12 for further details.) This shock interaction is practically not affected by viscous effects (except within the inner core recirculation). If viscous effects are not important, then the Euler theory tells us that the geometrical scale of the nozzles should have no influence. This is clearly demonstrated by the similar structures of the cap-shock pattern exhibited by the subsale and full-scale nozzles shown in Fig. 18 (similar gas composition presumed).

As discussed in detail, RSS was observed during start-up and shut-down in both nozzle extensions (Fig. 19). The transition in the C/SiC subscale nozzle extension occurred at exactly the same PR as observed on the full-scale Vulcain. The key driver for the transition process is the momentum balance of the flow across the oblique shock system of the cap-shock pattern (Ref. 12). Because of similar core gas properties and contour shapes, the cap-shock structure is nearly identical. At a given PR and presuming identical separation positions in both nozzles, the momentum balance is, therefore, practically not influenced by viscous effects. Thus, as demonstrated in the tests, no significant difference between both nozzle sizes was observed for the transition PR.

To demonstrate the capability of the discussed analytical model for the cap-shock structure prediction in hot-gas plumes, Fig. 20 shows a comparison of the model results with the Vulcain full-scale plume pattern shown in Figs. 18 and 19. The experimental full-scale plume shock structure at the nominal PR is extracted from photograph. However, no such image exists for the cap-shock pattern in the RSS condition because of the shock position being far inside the nozzle extension. As a consequence, the analytical results are

compared to the numerical simulation for the RSS structure. Because of its inviscid character, the model prediction of the corresponding cap-shock structures for the C/SiC subscale nozzle yields exactly the same shapes.

The prediction for the transitional side load of the Vulcain C/SiC subscale nozzle at the PR of $p_c/p_a = 40$ yields a value of 1/25th of the corresponding full-scale value:

$$\frac{F_{\text{sl,subscale}}}{F_{\text{sl,full-scale}}} \propto \frac{(\partial m/\partial t)_{\text{subscale}}}{(\partial m/\partial t)_{\text{full-scale}}} \propto \frac{\left(r^2_{\text{throat}}\right)_{\text{subscale}}}{\left(r^2_{\text{throat}}\right)_{\text{full-scale}}} = \left(\frac{1}{5}\right)^2$$

The transitional side load predicted with the model was close of the maximum measured Vulcain full-scale side load (within an inaccuracy of 2%, Table 2).

No side-load measurement was installed during the C/SiC subscale test campaign. Consequently, that experimental reference is not available. However, the predicted transitional side load just described was used as the load case for the mechanical design of the C/SiC subscale nozzle. That the nozzle withstood the transition without structural failure is an indirect confirmation that the model's transition side-load prediction was correct. Table 3 summarizes the essential findings from these comparisons.

Summary

Principle flow phenomena observed in full-scale engine testing, such as the cap-shock pattern in the plume of parabolic nozzles, or FSS and RSS during start-up and shut-down, may also be observed in subscale cold-gas experiments. Because of the low cost and ease in access for sophisticated diagnostic methods, this class of experiments is preferred for fundamental research aspects including screening of design aspects. The prediction of subscale test results as the basis for a potential full-scale design may be achieved by characteristic numbers used for normalization and analytical or numerical models. It was shown that for the transition in separation characteristic from FSS to RSS high accuracy may be achieved with analytical models that are based the physical process responsible for the specific flow behavior. This also includes the analytical prediction of the resulting side force. However, note that both effects, the transition and the resulting side load, mainly depend on the inviscid momentum balance across the cap-shock system.

Numerical methods are a fundamental help for understanding the flow physics, for example, for the cap-shock pattern. Furthermore, prediction of flow phenomena dominated by viscous effects, such as the wall heat flux predictions, have reached a high confidence level. This was demonstrated with a numerical scheme being carefully validated by test results that are relevant for the specific application. The comparison of experimental hot-gas test results with results from numerical simulations showed fairly good agreement for the heat transfer in the purely radiation-cooled nozzle extension.

A further quality in full-scale prediction accuracy may be achieved with subscale tests under representative combustion chamber operational conditions. This implies hot-gas flow with identical propellants, chamber pressures, and mixture ratios. The similarity between full-scale and subscale flow patterns was clearly demonstrated for the Vulcain nozzle, for which subscale test results at a one-fifth geometric scale were discussed in detail. For both nozzles, the plume pattern was the same, and the transition from FSS to RSS occurred at exactly the same PR.

This result strongly supports the importance of doing representative subscale hot-firing tests during development in general, especially for advanced nozzle concepts featuring highly transient separation characteristics. For example, to characterize the transition behavior from sea-level to vacuum operation in a dual-bell nozzle, the use of the same hot-gas flow properties would remove any uncertainty with respect to gas compositions, leaving the geometric dependency as the only remaining item of uncertainty. Currently it is questionable if the time required for transition and the resulting side force can be predicted with sufficient accuracy by analytical and/or numerical models that have only been validated by cold-gas test results.

Finally, the hot-fire test campaign of the advanced 40-kN thrust chamber entirely fulfilled the expectations in giving valuable experimental data to improve both the theoretical prediction and design tools.

Acknowledgments

The TEKAN and ASTRA are sponsored by the DLR, German Aerospace Research Center, Bonn, under Contracts 50TT9626 and 50JR0015. The authors thank the Contract Officers H. Brücker and H.-D. Speckmann for their cooperation. A part of the work presented in this paper has been performed within the framework of the European Flow Separation Control Devices Working Group. The authors acknowledge R. Stark (DLR), P. Reijasse (ONERA), T. Alziary (LEA Poitiers), R. Ryden, M. Frey, and T. Damgaard (Volvo Aero Corporation), P. James (SNECMA), J. Muylaert, and R. Schwane (ESA, European Space Research and Technology Centre), and M. Pons, and P. Vuillermoz (Centre National d'Etudes Spatiales) for their cooperation. The authors appreciate the teamwork of Astrium, engineers involved in this program, especially H. Immich, J. Kretschmer, F. Grauer, and M. Terhardt.

References

[1]Immich, H., Kretschmer, J., and Preclik, D., "Thrust Chamber Technology Development for Future Launch Vehicle Liquid Rocket Engines," *37th AIAA Joint Propulsion Conference*, AIAA Paper 2001-4841, Salt Lake City, July 2001.

[2]Immich, H., Kretschmer, J., and Preclik, D., "Technology Developments for Cryogenic Rocket Engines," *36th AIAA Joint Propulsion Conference*, AIAA Paper 2000-3780, Huntsville, July 2000.

[3]Hagemann, G., Immich, H., Dumnov, G., and Nguyen, T., "Advanced Rocket Nozzles," *Journal of Propulsion and Power*, Vol. 14, No. 5, 1998, pp. 620–634.

[4]Hagemann, G., Terhardt, M., Haeseler, D., and Frey, M., "Experimental and Analytical Design Verification of the Dual-Bell Concept," *Journal of Propulsion and Power*, Vol. 18, No. 1, 2002, pp. 116–122.

[5]Stark, R., Hagemann, G., Kwan, W., and Terhardt, M., "Rocket Nozzle Cold-Gas Test Campaigns for Plume Investigations," *Proceedings of the 4th European Symposium on Aerothermodynamics for Space Vehicles*, ESA SP-487, Dec. 2001, pp. 611–618.

[6]Hagemann, G., Immich, H., and Dumnov, G., "Critical Assessment of the Linear Plug Nozzle Concept," *37th AIAA Joint Propulsion Conference*, AIAA Paper 2001-4865, Salt Lake City, July 2001.

[7]Dexter, C. E., "ALS LOX/H2 Subscale Coaxial Injector Testing," AIAA Paper 91-1871, June 1991.

[8]Howell, D. J., Petersen, E. L., and Clark, J. A., "Performance Characteristics of LOX/H2, Tangential-Entry, Swirl-Coaxial, Rocket Injectors," AIAA Paper 93-0228, Jan. 1993.

[9]Hagemann, G., Terhardt, M., Frey, M., Reijasse, P., Onofri, M., Nasuti, F., and Östlund, J., "Flow Separation and Side-Loads in Rocket Nozzles," *4th International Symposium on Liquid Space Propulsion*, DLR, Lampoldshausen, Germany, 2000.

[10]Terhardt, M., Hagemann, G., and Frey, M., "Flow Separation and Side-Load Behavior of the Vulcain Engine," *35th AIAA Joint Propulsion Conference*, AIAA Paper 99-2762, Los Angeles, June 1999.

[11]Frey, M., and Hagemann, G., "Restricted Shock Separation in Rocket Nozzles," *Journal of Propulsion and Power*, Vol. 16, No. 3, 2000, pp. 478–484.

[12]Frey, M., Hagemann, G., and Koschel, W., "Appearance of Restricted Shock Separation in Rocket Nozzles," *Journal of Propulsion and Power*, Vol. 18, No. 3, 2002, pp. 577–584.

[13]Frey, M., Stark, R., and Ciezki, H., "Subscale Nozzle Testing at the P6.2 Test Stand," *36th AIAA Joint Propulsion Conference*, AIAA Paper 2000-3777, Huntsville, July 2000.

[14]Preuss, A., "An Analytical Approach for the Flowfield Analysis of Overexpanded Rocket Nozzles," International Astronautical Federation, Paper IAF-00-W.2.08, Oct. 2000.

[15]Mattsson, J., Högman, U., and Torngren, L., "A Subscale Test Programme on Investigation of Flow Separation and Side-Loads in Rocket Nozzles," *Proceedings of the 3rd European Symposium on Aerothermodynamics for Space Vehicles*, ESA SP-426, Jan. 1999, pp. 373–378.

[16]Östlund, J., and Bigert, M., "A Subscale Investigation on Side-Loads in Sea Level Rocket Nozzles," *35th AIAA Joint Propulsion Conference*, AIAA Paper 99-2759, Los Angeles, June 1999.

[17]Reijasse, P., Servel, P., and Hallard, R., "Synthesis of the 1998-1999 ONERA Works in the FSCD Working Group," ONERA, Rept. RTS 49/4361 DAFE/Y, Dec. 1999.

[18]Östlund, J., Damgaard, T., and Frey, M., "Side-Load Phenomena in Highly Overexpanded Rocket Nozzles," *37th AIAA Joint Propulsion Conference*, AIAA Paper 2001-3684, Salt Lake City, July 2001.

[19]Reijasse, P., Morzenski, L., Blacodon, D., and Birkemeyer, J., "Flow Separation Experimental Analysis in Overexpanded Subscale Rocket Nozzles," *37th AIAA Joint Propulsion Conference*, AIAA Paper 2001-3556, Salt Lake City, July 2001.

[20]Manski, D., and Hagemann, G., "Influence of Rocket Design Parameters on Engine Nozzle Efficiencies," *Journal of Propulsion and Power*, Vol. 12, No. 1, 1996, pp. 41–47.

[21]Alting, J., Grauer, F., Hagemann, G., and Kretschmer, J., "Hot-Firing of an Advanced 40 kN Thrust Chamber," *37th AIAA Joint Propulsion Conference*, AIAA Paper 2001-3260, Salt Lake City, July 2001.

[22]Nickerson, G. R., Dang, L. D., and Coats, D. E., "Two Dimensional Kinetic Reference Computer Program TDK," *Engineering and Programming Manual*, Rept. NAS8-35931, April 1985.

[23]Dumnov, G. E., "Unsteady Side-Loads Acting on the Nozzle with Developed Separation Zone," *32nd AIAA Joint Propulsion Conference*, AIAA Paper 96-3220, Lake Buena Vista, July 1996.

[24]Alting, J., "Investigation of Shock/Boundary Layer Interactions in Rocket Engine Nozzles," DLR, German Aerospace Research Center, Rept. DLR IB-645-98/13, July 1998 (in German).

[25]Schmucker, R. H., "Status of Flow Separation Prediction in Liquid Propellant Rocket Nozzles," NASA TM X-64890, Nov. 1974.

[26]Terhardt, M., Hagemann, G., and Frey, M., "Flow Separation and Side-Load Behavior of Truncated Ideal Rocket Nozzles," *37th AIAA Joint Propulsion Conference*, AIAA Paper 2001-3686, Salt Lake City, July 2001.

[27]Knab, O., Fröhlich, A., and Wennerberg, D., "Design Support for Advanced Storable Propellant Engines by ROCFLAM Analyses," *35th AIAA Joint Propulsion Conference*, AIAA Paper 99-2459, Los Angeles, June 1999.